CARBON 50 (2012) 3789–3798

Available at www.sciencedirect.com

SciVerse ScienceDirect

journal homepage: www.elsevier.com/locate/carbon

Impact of nanotube density and alignment on the elastic modulus near the top and base surfaces of aligned multi-walled carbon nanotube films

Yuan Gao [a,*], Takashi Kodama [a], Yoonjin Won [a], Senyo Dogbe [b], Lawrence Pan [c], Kenneth E. Goodson [a]

[a] Department of Mechanical Engineering, 440 Escondido Mall, Stanford University, Stanford, CA 94305, USA
[b] Stanford Nanofabrication Facility, Paul G. Allen Building, 420 Via Palou Mall, Stanford University, Stanford, CA 94305, USA
[c] Molecular Nanosystems Inc., 977 Commercial Street, Palo Alto, CA 94303, USA

ARTICLE INFO

Article history:
Received 24 February 2012
Accepted 2 April 2012
Available online 13 April 2012

ABSTRACT

The mechanical compliance of vertically aligned carbon nanotube (VACNT) films renders them promising as interface materials that can accommodate thermal expansion mismatch. Here we study the relationship between the detailed morphology and elastic modulus of multi-walled VACNT films with thicknesses ranging from 98 to 1300 μm. A systematic analysis of scanning electron micrographs reveals variations in nanotube alignment and density among samples and within different regions of a given film. Nanoindentation of both top and bottom film surfaces using an atomic force microscope with spherical indenters with radii between 15 and 25 μm provides evidence of the modulus differences. The top surface is shown to have a higher modulus than the base, with out-of-plane modulus values of 1.0–2.8 MPa (top) and 0.2–1.4 MPa (base). The indentation data and microstructural information obtained from electron microscopy are interpreted together using an open cell foam model to account for differences in nanotube alignment and density, which are generally lower at the base and yield predictions that are consistent with the modulus data trends. This work shows that microstructure analysis complements property measurements to improve our understanding of nanostructured materials.

1. Introduction

The thermal resistance and reliability of thermal interface materials (TIMs) are critical limiting factors for a variety of technologies including electronics thermal management and thermoelectric energy conversion [1,2]. Vertically aligned carbon nanotube (VACNT) films offer great promise as TIMs because they offer high through-plane thermal conductance and mechanical compliance. VACNT films typically have a complex, entangled nanotube structure and morphological details such as the density, alignment, and tortuosity of CNTs within a film affect the mechanical and thermal properties of the film. Given the variety of growth techniques and variations in film morphology, it is important to understand how these factors influence film behavior as TIMs. VACNT films will need to be released from their growth substrate and attached to the device being cooled, so released films must also be characterized.

While there has been considerable work on measuring the thermal performance of VACNT films [3,4], the mechanical properties need more attention. Past research on the mechanical properties of VACNT films yielded a wide variety of

* *Corresponding author:* Fax: +1 650 7237657.
E-mail address: yuangao@stanford.edu (Y. Gao).
0008-6223/$ - see front matter
http://dx.doi.org/10.1016/j.carbon.2012.04.004

Nomenclature

A	area, m^2
B	relative modulus factor, Pa
C	a constant
E	Young's modulus, Pa
e	geometric constant used in Oliver–Pharr analysis
F	force, N
f	volume fraction
H	unit cell height, m
h	tip displacement into the sample, m
I	moment of inertia, m^4
k	spring constant, N/m
L	unit cell width and length, m
l	length of a CNT in a unit cell, m
P	load, N
R	radius, m
S	contact stiffness, N/m
x	cantilever deflection, m

Greek symbols

α	aspect ratio
γ	work of adhesion, mJ/m^2
Δ	unit cell vertical deflection, m
ε	strain
θ	CNT angle in a unit cell
ν	Poisson's ratio
σ	stress, N/m^2

Subscripts

1	in-plane
2	out-of-plane
adh	maximum adhesion force
base	bottom surface of film
c	contact depth
f	film
i	indenter
in	inner radius of a CNT
max	total displacement below film surface
out	outer radius of a CNT
r	reduced modulus
rel	relative modulus
s	single tube
top	top surface of film

out-of-plane modulus (E_2) values ranging from below 10 MPa to hundreds of MPa [5–13], likely due to the variety of film structures and measurement techniques. These prior work often assumed that the film structure is homogeneous, which is in contrast with the strongly varying in-plane modulus (E_1) we reported recently for multi-walled VACNT films of thicknesses between 0.5 and 100 μm [14] based on both scanning electron microscopy (SEM) images and thickness-dependent modulus data obtained using a novel resonator technique. This suggests that understanding and quantifying the inhomogeneous morphology of VACNT films in conjunction with elastic modulus measurements will improve data interpretation and analysis.

Several studies quantified the morphology of VACNT films using image analysis or X-ray scattering techniques [15–19]. There is often a thin, highly-entangled crust layer, followed by a more vertically aligned middle section, followed by a disordered, lower density base region. The distinction between these regions tends to be more pronounced for films much thicker than ~10 μm [16]. Some studies observed a relationship between the tortuosity of VACNT films and measured modulus [7,18], while others observed that buckling always begins at the film base during uniform compression [8,10–12,20,21]. These studies indicate that the film microstructure strongly influences the mechanical properties of the film. Yet none use quantitative microstructure analysis of the film to predict mechanical behavior.

The present work extracts the localized out-of-plane mechanical modulus of five multi-walled VACNT films with thicknesses ranging from 98 to 1300 μm through nanoindentation by an atomic force microscope (AFM). Previous work used AFM nanoindentation on a well-aligned CNT film to measure individual CNT properties by using a sharp pyramidal tip to penetrate between the tubes [22]. Instead, we use spherical indenter tips with radii between 15 and 25 μm to measure bulk behavior rather than individual tubes. We measure the differences in E_2 between the top and bottom regions, which often have different morphologies. The modulus on the top side ($E_{2,top}$) is measured on as-grown films. The modulus at the bottom surface ($E_{2,base}$) is measured by releasing the film from the substrate and indenting from the backside. In this way we can observe the inhomogeneous mechanical behavior within VACNT films and compare the results between films of different thicknesses. Image analysis performed on SEMs of the samples quantifies their alignment and density. These values are input into a cellular mechanical model to compare predicted behavior to measurement results.

2. Experimental procedure

2.1. Material preparation

This work investigates five multi-walled VACNT films grown under similar conditions with final film thicknesses of 98, 150, 200, 205, and 1300 μm. The growth process and density measurement procedures are detailed in Won et al. [14]. The mass densities range from 0.029 to 0.056 $g\,cm^{-3}$ which translates to 1.3–2.5% volume fraction (f) assuming an individual multi-walled CNT density near graphite of 2.2 $g\,cm^{-3}$. To indent the films on the base side, the VACNT films are released from the substrate by first placing the top of the film on a thin layer of carbon paste (Structure Probe, Inc.) on a second substrate and then pulling the original substrate off after the adhesive dries (Fig. 1a). Carbon paste is used for this study because it is SEM compatible and easy to apply, though in actual

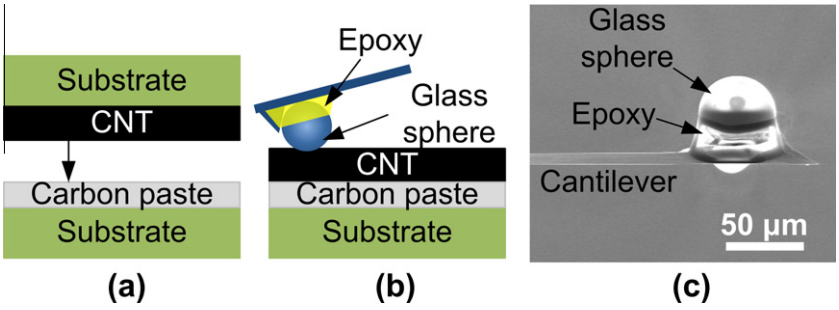

Fig. 1 – (a) Schematic of the VACNT film release procedure for measurements of the base side modulus. The top of the original film is bonded to a new substrate using carbon paste. (b) Schematic of an indenter at the base surface of a VACNT film that has been bonded to a new substrate. (c) SEM of the indenter tip. The original AFM tip which is nominally 17 μm tall is located to the right of the glass sphere and is partially covered with epoxy. The white shadows in the image are due to charging effects during imaging.

TIM applications the film can be bonded and released with a binder metal to enhance thermal conduction [23]. The carbon paste is viscous and there is little wicking into the film. To avoid changing the film's microstructure, minimal pressure is applied when bonding the film. Each released sample is inspected under SEM and samples with significant damage are not used in the study. Fig. 1b illustrates the indentation of the flipped film.

Fig. 1c shows an SEM image of an indenter consisting of a 25 μm diameter glass microsphere (Polysciences, Inc.) attached to the end of a tapping-mode AFM cantilever (TAP-190AL-G, BudgetSensors). Three different indenter tips are used in this study with spheres of radii 15, 20, and 25 μm determined using SEM images. The large diameter ensures sampling of bulk film properties rather than individual nanotubes. Tubes are typically spaced ~100 nm apart and a sharp AFM tip will penetrate the surface and push tubes laterally. Unlike sharp indenters the large radius also allows accurate determination of the tip geometry for the force curve analysis. Compared with flat indenters the spherical probe does not need to be aligned perfectly perpendicular to the surface of the sample. The glass indenter tip ($E \sim 70$ GPa) is much harder than the films being investigated ($E < 10$ MPa).

The spring constant k of each cantilever is calculated using the Sader method [24] before attachment of the glass spheres. For this calculation a laser Doppler vibrometer is used to find the quality factor and resonant frequency of each AFM cantilever and the cantilever width and length are measured using SEM images. The measured k values range from 17 to 20 N/m. The glass spheres are first cleaned using a Piranha solution to remove surface residue. Then spheres are attached with epoxy to each cantilever based on the method described in Kodama et al. [25].

2.2. *Measurement methods*

VACNT films with entangled morphologies have been shown to behave as a foam-like network of tubes rather than independent, vertical CNTs since there are significant tube-tube interactions due to van der Waals forces [5,7–8,11,12,16]. Previous observations of base-side buckling behavior in VACNT films involved uniaxial compressions with minimal lateral forces [8,10–12,20,21]. In those measurements the film essentially acts as a series of vertical springs and the weakest layer (typically the base) deforms the most regardless of the direction of indentation. Nanoindentation measurements of VACNT films result in a localized response similar to that of solid materials [8], providing the capability to measure properties at the top and base regions. Studies on indentation of multilayer structures showed that the measured modulus is progressively affected by each layer and varies with penetration depth [26,27]. Since VACNT alignment is gradually changing with depth, the measured moduli are an average of the local properties at the top and base, though the indentations are kept shallow and do not show a significant change in modulus with depth.

The elastic modulus of each VACNT film in this work is measured using a Topometrix Explorer scanning probe microscope capable of force measurements. These microscopes provide high sensitivity to load and displacement and have been previously used to measure the mechanical properties of a variety of materials, including polymers and biological materials, yielding information about local material properties such as hardness, elasticity, and adhesion [28,29]. AFMs are especially useful for observing soft, fragile samples and allow for use of a variety of indenter sizes, materials, and cantilevers.

To obtain an accurate load-depth curve a number of calibration and conversion steps are performed. The piezoactuator is calibrated to account for nonlinearity, hysteresis, and creep between the applied voltage and displacement [30]. For each measurement, the conversion of photodiode voltage to cantilever free-end deflection is determined by pressing the tip on a hard sample such that there is no penetration into the sample. The cantilever deflection is converted to force F using $F = k^*x$ where x is the cantilever deflection. Because the loading force is affected by the tilt of the AFM cantilever with respect to the sample, a correction factor given in Heim et al. [31] is applied which also accounts for indenter size. During the measurement the tip deflection is kept within the linear region of the photodetector. The data are taken using a tip velocity of 4 μm/s which is sufficiently fast to render the data independent of velocity. The actual load signal resolution depends on the range of indentation and number of data points taken but remains below 20 nm in displacement and 8 nN in force.

The Young's modulus of the material can be determined from the load-depth curve using the Oliver–Pharr method [32], which is appropriate for elastic–plastic materials and has been previously used on other measurements of VACNT films which exhibit this behavior [6–8]. The slope of the initial unloading curve, S, represents purely elastic recovery and is a measure of the contact stiffness $S = dP/dh$ where P is the load and h is the displacement. To find S, the initial portion of the unloading curve is fit to a power law relation. S is related to the reduced modulus E_r by

$$E_r = \frac{S}{2}\frac{1}{\sqrt{2h_cR_i - h_c^2}}, \quad (1)$$

where R_i is the radius of the indenter and h_c is the actual contact depth given by

$$h_c = h_{max} - e\frac{P_{max}}{S}. \quad (2)$$

Here h_{max} is the total indentation depth below the surface of the film and e is a geometrical constant equal to 0.75 for a paraboloid of revolution. The initial contact point is determined from the point where the force curve deviates from the zero force line. There is some error in choosing the location of this contact point, but the results are not strongly sensitive to h_{max}. The modulus of the film is calculated from E_r using

$$E_r = \left[\frac{1-\nu_i^2}{E_i} + \frac{1-\nu_f^2}{E_f}\right]^{-1} \quad (3)$$

where E_i, ν_i, and E_f, ν_f represent the Young's modulus and Poisson's ratio of the indenter (glass sphere) and substrate (VACNT film), respectively. The value of E_i and ν_i used for glass are 70 GPa and 0.2, respectively. The value of ν_f for VACNT films is commonly assumed to be zero since the response is similar to a foam material [8,11].

The Oliver–Pharr method does not include adhesion effects, which are significant for measurements on the base of the film and can yield error in the analysis [33]. The top surface may have lower adhesion than the base due to the entangled crust layer, which reduces engagement of the CNTs to the contacting surface [34,35]. Thus data for the base of the film are also analyzed using Johnson–Kendall–Roberts (JKR) adhesion theory [36]. According to the Tabor parameter, the JKR model is valid for these samples, which are compliant, elastic materials with high surface energy and measured with large radii indenters [37]. Fitting the force curve to the model gives E_2 and the work of adhesion $\gamma = 2P_{adh}/(3\pi R_i)$ of the sample, where P_{adh} is the maximum adhesion force [33].

Since the samples are porous, they have high surface roughness, on the order of 100 nm and 1 μm root mean square roughness for the top and base respectively based on AFM topography scans. The roughness may be lower for the top because of the horizontally-aligned tubes in the crust layer, whereas the released base consists of vertical CNT tips. Past work showed that roughness results in an underestimated modulus and scattered data, and that its effects diminish with indentation depth [38,39]. We mitigate errors due to roughness by averaging results from different locations and indenting deeper than the surface roughness. The average indentation depth for the samples ranges from 600 to 1160 nm for the top surface and 2.17–6.62 μm for the base, corresponding to 0.09–0.80% strain for the top and 0.3–3.0% strain for the base. The maximum indentation depth of each sample is at least 10 times less than the total thickness of the VACNT film to avoid influence from the Si substrate [32]. Measurements are taken on each sample using at least two different indenter tips and at least five different locations for each tip for a total of over 10 indentations per sample. There is no significant difference in measurement results between tips. Measurements are not repeated at the same location due to the stress softening behavior of the film [10,40].

Indentation of rough surfaces can be divided into two steps: flattening of the asperities and then indentation of the flattened surface [41]. As shown in Fig. 4c, the "free" tips of the base-side nanotubes deform plastically to form a flattened surface against the indenter tip, creating a profile similar to a crust layer. During applied load the base side experiences a greater increase in CNT-indenter contact area than the top, which may lead to greater underestimation of $E_{2,base}$ than $E_{2,top}$. Since we cannot observe the progression of contact area during indentation, we estimate this effect by changing the initial contact point in the analysis such that the loading begins after the flattening of the base side tips. This reflects the extreme case of no contact before this point, simulating extremely sparse CNT tips. For a 20% lower h_{max}, E_2 calculated using the Oliver–Pharr method increases proportionally by 20%. However, E_2 calculated using the JKR method only increases by 3%. Thus the deep indentations and JKR analysis reduce the underestimation of $E_{2,base}$.

The measurement system is verified using a 1 mm-thick polydimethylsiloxane (PDMS) 10:1 reference sample (Sylgard 184, Dow Corning Inc.). The Poisson ratio of PDMS is assumed to be 0.5. The measured modulus values are 1.3 ± 0.2 MPa which match well to past work that reported ~1.5 MPa elastic modulus [42,43].

2.3. *Cellular model*

Past literature has shown that the mechanical response and microstructure of VACNT films can be effectively modeled as an open-cell foam [10,11]. Open-cell foams have been previously analyzed using dimensional relations between the mechanical modulus and a measure of the physical structure (e.g., unit cell size) since the variation in pore size and geometry makes it difficult to create an exact model. These relations have excellent fit to data down to a constant of proportionality [44]. For this analysis we use a simple three-dimensional open-cell foam model similar to the work of Gibson et al. [44] to simulate the mechanical response of the VACNT foam using dimensional relations.

Fig. 2a shows a unit cell comprised of eight CNT sections of length l oriented at an angle θ to the plane of the film. The unit cell has height H and length and width L to account for modulus anisotropy between the CNT growth direction (out-of-plane) and in-plane directions. The aspect ratio α is defined as $\alpha = H/L = \sqrt{2}\tan\theta$. Fig. 2b shows a single angled tube segment from which the relationships $H = 2l\sin\theta$ and $L = \sqrt{2}l\cos\theta$ are derived. The cellular model does not capture the variety of complex tube interactions such as tube-tube

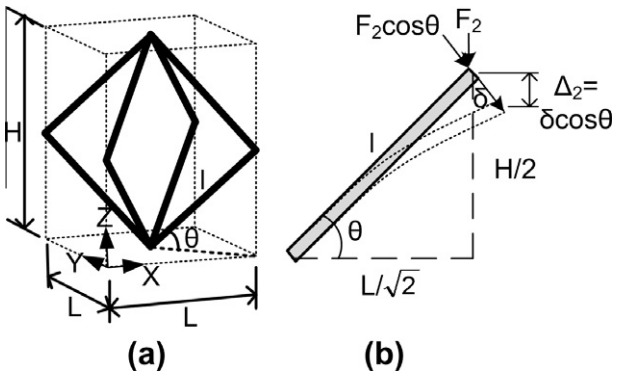

Fig. 2 – (a) Anisotropic unit cell where $H > L$. H is the growth (out-of-plane) direction. The nanotubes are hollow cylinders represented by the thick solid lines of length l. (b) Diagram of a single tube with a vertical force F_2. The beam is deflected by Δ_2 in the vertical direction.

bundling and van der Waals forces in the structure, but the results of this model match well to a coarse-grained molecular simulation of the film structure that does account for those effects over a wide range of α and f [1].

The present analysis assumes that the VACNTs act as Euler–Bernoulli beams. For E_1, a horizontal force F_1 is applied at the end of each beam and for E_2, a vertical force F_2 is applied at the end of each beam (shown in Fig. 2b). The resulting in-plane and out-of-plane strains ε_1 and ε_2 are

$$\varepsilon_1 = \frac{\Delta_1}{L/2} \propto \frac{F_1 l^3 (2 - \cos^2\theta)}{E_s I L} \tag{4}$$

$$\varepsilon_2 = \frac{\Delta_2}{H/2} \propto \frac{F_2 l^3 \cos^2\theta}{E_s I H}. \tag{5}$$

Here Δ_1 and Δ_2 are the beam deflections in the in-plane and out-of-plane directions respectively. I is the principal moment of inertia. $I = \pi\,(R_{out}{}^4 - R_{in}{}^4)/4$ where R_{out} is the outer radius of a CNT and R_{in} is the inner radius. E_s is the Young's modulus of an individual CNT, which is typically ~1 TPa [45]. The total stress on the cell in the in-plane direction, σ_1, and out-of-plane direction, σ_2, is $4F_1/LH$ and $4F_2/L^2$, respectively.

The volume fraction f can be expressed as the relative volume occupied by the nanotubes in a unit cell.

$$f = \frac{8lA}{L^2 H} = \frac{2A}{l^2 \cos^2\theta \sin\theta}. \tag{6}$$

Here A is the cross-sectional area of an individual CNT. After substituting l with f in Eq. (4) and (5), E_1 and E_2 become functions of θ,f, and individual tube properties:

$$E_1 = \frac{B \cos^4\theta \sin\theta}{2 - \cos^2\theta} \tag{7}$$

$$E_2 = B \sin^3\theta \tag{8}$$

$$B = \frac{C E_s I f^2}{A^2}. \tag{9}$$

The values of f and α (where $\alpha = \sqrt{2}\tan\theta$) are calculated for each indented region using the image analysis procedure described in the next section. B is defined to factor out the dependence on f, since each region of the VACNT film has a different α and f and we want to isolate the dependence of E_2 on α. The measured E_2 are converted to a relative modulus $E_{2,rel} = E_2/B$. Then $E_{2,rel}$ is compared to the predicted trend, $\sin^3\theta$ (Eq. (8) divided by B). Since these are dimensional relationships, C is defined as a constant of proportionality which is determined by using a least squares fit between the data and model.

2.4. *Image analysis*

Image analysis techniques are used to estimate H and L at various locations in a cross-sectional SEM image of the VACNT film to detect morphological variations. For image analysis, the VACNT samples are first cleaved to gain visual access to the nanotubes away from the sample edges. The cleaved edge is sputter coated with ~4 nm Au to increase SEM image contrast. The image analysis technique is insensitive to the tube diameters. All images of the film are taken using a FEI XL30 Sirion SEM at 150 kX magnification under identical microscope settings. This provides the best images for analysis in terms of capturing a large area with adequate resolution, as shown in Fig. 3a, and keeps the depth of field constant. An image at this magnification covers roughly a 1.5×2 μm area.

Binarization of the SEM images using thresholding (the Otsu method) limits the image to a thin plane since brightness decreases with depth. Slight variations in threshold value do not have a significant effect on the results. If a large portion of the image is not in the same plane, that area is cropped out. Image processing operations are used to remove noise and large specks. An example of the final binary image is shown in Fig. 3b. The intersections between the nanotubes and 50 evenly spaced probe lines are counted in both the horizontal and vertical directions, as in Fig. 3c and d. This is a standard stereological procedure for quantifying geometries in a cross-sectional image [46], and the number of probe lines do not significantly affect the results above a certain point. The average tube-tube spacing is calculated by dividing the total probe line length by the total number of intersections. The measured tube-tube distance in the horizontal and vertical directions are converted to 3D cell dimensions L and H using a factor of 1.5 [44] which are then converted to f and α using the cellular model. The factor gives the appropriate film f of ~2% as determined from the mass density measurements.

3. Results and discussion

The crust, top, middle, and base regions within a typical VACNT film are indicated in Fig. 4a. Fig. 4b shows the flipped film attached with carbon paste to a secondary substrate. Fig. 4c shows the released surface with an indented region (see dis-

[1] Won Y, Gao Y, Panzer MA, Goodson KE. Zipping, Entanglement, and the Modulus of Aligned Single-Walled Carbon Nanotube Films. Unpublished. 2012.

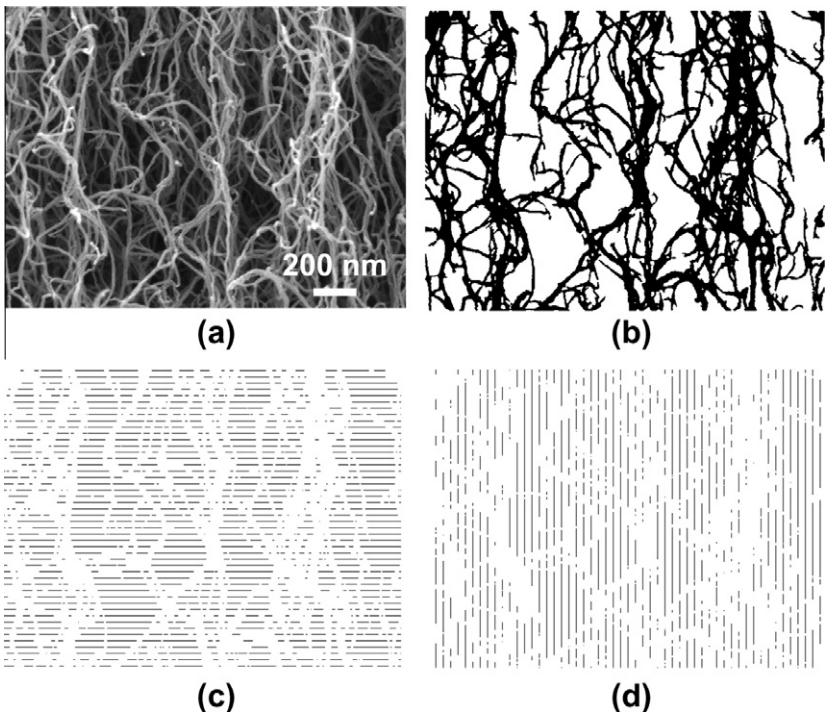

Fig. 3 – (a) An SEM is taken of a section of the VACNT film that is roughly in one plane. (b) The binary image after filtering. (c) Horizontal and (d) vertical straight probe lines drawn across the binary image to detect intersections with nanotubes.

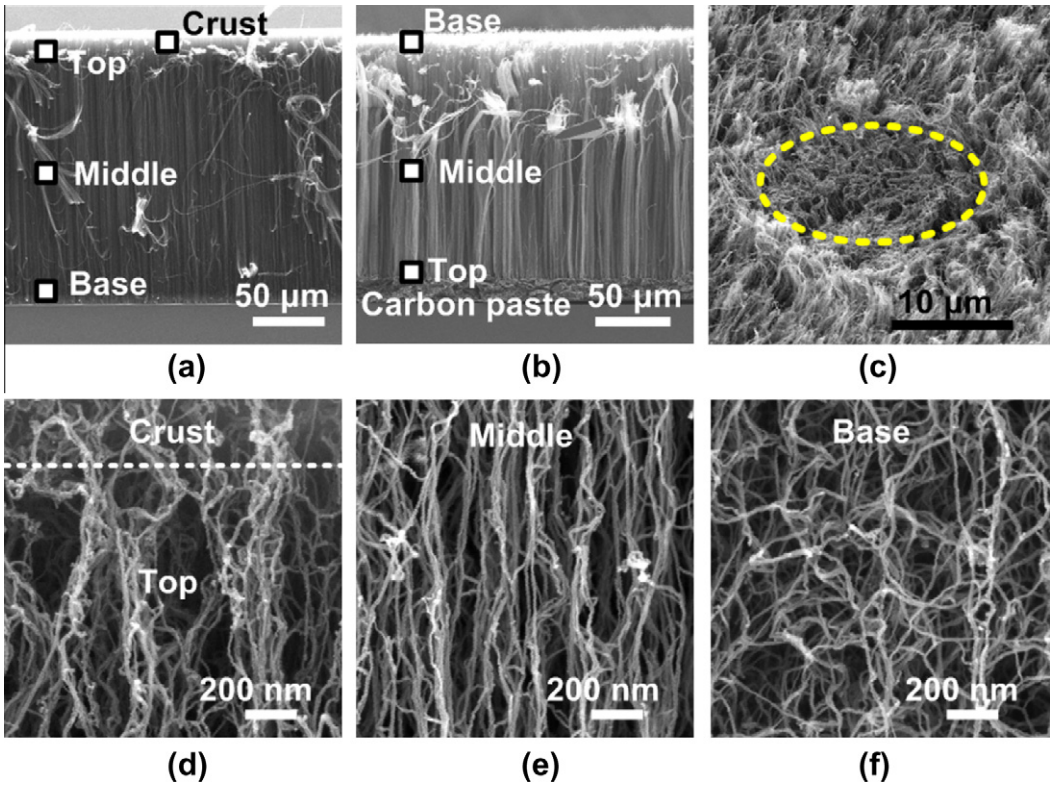

Fig. 4 – (a) Cross-sectional micrograph of a 200 μm-thick VACNT film showing locations of the crust, top, middle, and base regions. The crust is directly above the top region. (b) The released and flipped film on carbon paste with the original regions reversed. (c) SEM image of a 45° view of a released base surface with a region of plastically deformed CNT tips (circled) from indentation. The released surface has no crust layer. (d) SEM images of the crust and top, (e) middle, and (f) base regions showing the differences in CNT morphology.

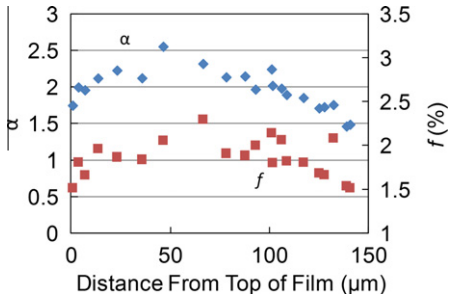

Fig. 5 – Image analysis results for the 150 μm-thick sample showing aspect ratio (α, diamonds) and volume fraction (f, squares) calculated from SEM images as a function of depth into the sample. Zero distance corresponds to the top of the film. In each region, over all samples the standard deviation of α and f is between 3–12% and 5–18%, respectively. These results are used as inputs to the cellular model.

cussion of roughness, Section 2.2). The crust on the original film, shown in Fig. 4d, is ~200 nm thick for these films, which is too thin to analyze reliably using the image analysis procedure. As discussed later this crust layer does not significantly affect the modulus measurement. The images used for analysis are taken immediately below the crust in the top region. Fig. 4e and f depict the well-aligned middle and entangled base regions.

These trends are also reflected in Fig. 5 which shows the quantified tube structure using the image analysis procedure. The result shows that α peaks in the middle region and is equal or lower at the base than the top. Similar trends exist for all the samples and are akin to past observations [16]. The values of f are more scattered but are overall slightly higher at the top than the base.

The images of the released films are also analyzed to determine if the release procedure changes the film morphology. The morphology of the flipped films matches the original film within the scatter of the data. For comparison to measured data, at least three images are taken at the top of the original sample and base of the flipped sample respectively (the locations indented) to find the average cell dimensions. This ensures that any morphology change due to the release procedure is captured in the results.

Fig. 6 shows the force–displacement curves for (a) the top surface of the unmodified 150 μm-thick sample and (b) the base surface of the sample after release. The curve shapes are typical of all the samples. The tilt of the curve at negative depth is due to the movement of the tip above the sample, an artifact of the AFM setup. The hysteresis is a signature of energy dissipation, consistent with past observed behavior [8–12]. The dip below zero force reflects adhesion between the tip and sample. The base of the films has much higher adhesion than the top surface, as described in the methods section. Due to the shallow indentations and low forces, the majority of the indentations are in the linear regime of the stress–strain response of the film, as shown in Fig. 6c. Occasionally, for some deeper indentations at the base surface, the stress–strain curve levels off, indicating the initiation of buckling. This effect typically occurs between 8 and 20 kPa and reflects the soft nature of the base region. The top surface indentations remain in the linear regime through 80 kPa of stress.

Fig. 7 shows that for the indentation measurements $E_{2,base}$ is significantly lower than $E_{2,top}$. The modulus slightly decreases with film thickness, suggesting that thicker films are more misaligned, particularly at the base of the film. This is also consistent with previous observations [16]. The values of $E_{2,base}$ in Fig. 7 are calculated using the JKR analysis. The values of γ for the base surface range from 1.4 to 33 mJ/m^2 and are comparable to past work which showed γ between 20 and 80 mJ/m^2 for multi-walled VACNT films contacting a convex glass surface [34]. Not all the indentation curves give perfect fits to the JKR model, but the results for elastic modulus are consistent and the variations are reflected in the standard deviation.

For the range of indentation depths and the amount of variation in the data, the samples do not show a clear depth-dependent modulus. This indicates that the crust layer does not affect the response because it is negligibly thin or does not have a significantly different modulus than the top.

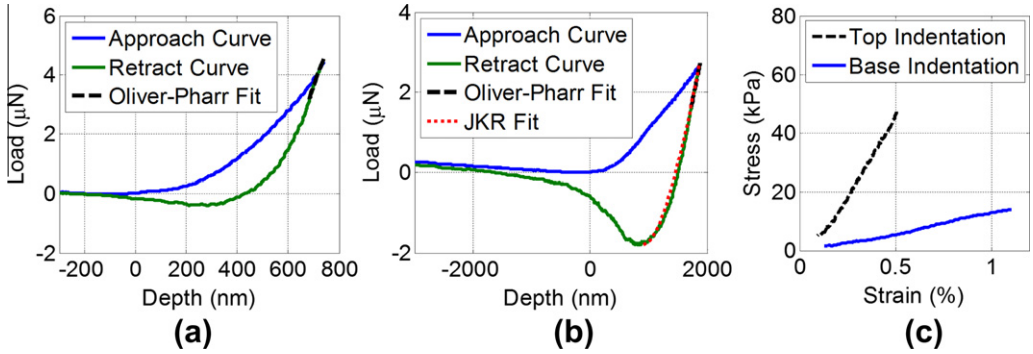

Fig. 6 – (a) Load-depth curve for the 150 μm-thick sample. "Approach Curve" corresponds to the response as the tip approaches the sample surface, and "Retract Curve" corresponds to the response of the tip moving away from the sample. The black dashed line represents the fitted slope used in the Oliver–Pharr analysis. (b) Load-depth curve for the released 150 μm-thick sample. The curve for the JKR model fit is also shown as the red dotted line. (c) Stress–strain plot of indentation from the top (dashed) and base (solid) of the 150 μm-thick sample. The contact area for the stress is calculated as described in the Oliver–Pharr method, $A = \pi(2h_cR - h_c^2)$ [32].

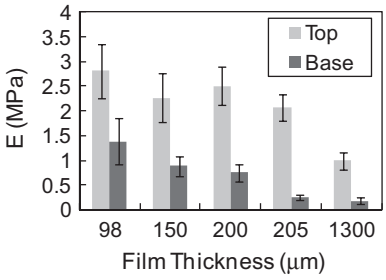

Fig. 7 – Elastic modulus measured from the top ($E_{2,top}$) and base ($E_{2,base}$) surfaces of VACNT samples of varying thicknesses. The error bars correspond to the standard deviation of the data.

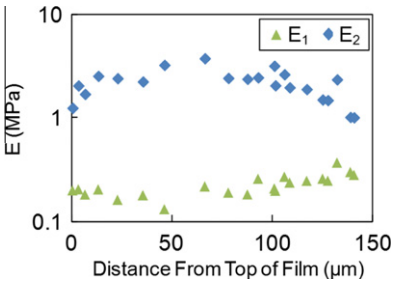

Fig. 9 – Predicted E_1 and E_2 of the 150 μm-thick sample as a function of depth into the sample using the cellular model and image analysis. The vertical axis has a log scale to depict trends in E_1.

According to the cellular model and supported by results in Won et al. [14], if the crust has nanotubes with mostly horizontal alignment it will have low E_2 though E_1 is high. The lack of depth-dependence also suggests that the indentations at both surfaces do not sample the properties of the well-aligned middle region.

To investigate the dramatic difference between $E_{2,top}$ and $E_{2,base}$, the cellular model is used to compare these values to the film morphology at the top and base. Fig. 8 shows $E_{2,rel}$ plotted against α for each data point, after accounting for differences in f. As mentioned earlier, α and f are generally equal or lower at the base region (filled data points) than the top (unfilled data points). Though the data is scattered, there is an overall trend of increasing $E_{2,rel}$ with α which suggests that the tube morphology may have a strong impact on the film mechanical properties.

In Fig. 8 these data points are also plotted against the theoretical curve calculated from the cellular model. The overall trend of increasing modulus with alignment matches the data, though the data increases more rapidly with α than predicted. For a number of reasons, $E_{2,rel}$ of the base side may be lower than expected. The image analysis procedure may not be sufficiently effective at detecting density differences due to the depth of field of the SEM, causing errors in f if the base is actually less dense than it appears [16]. The number of defects in a CNT may increase with growth time (as reflected by the increased tortuosity) which may reduce the magnitude of E_s in the base region. There is also the possibility of unobserved weakening of the film due to the release procedure for certain samples, such as the two thickest samples. The methods to overcome these shortcomings are beyond the scope of this paper and may be resolved by measurements of more samples with a wider range of α. These results do show that a simple cellular model can explain trends in film behavior based on the morphology of the tube structure.

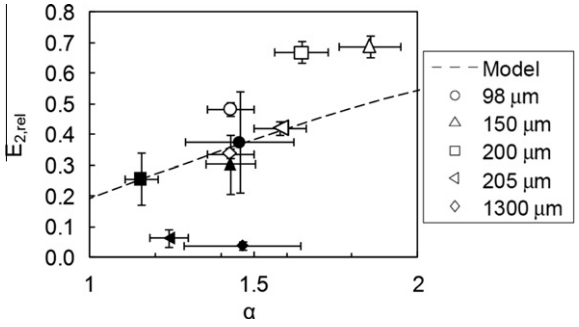

Fig. 8 – Measured modulus for all samples, represented by their thicknesses. Unfilled data points represent $E_{2,rel}$ of the top surface and filled data points (corresponding to the same samples as their unfilled counterparts) represent $E_{2,rel}$ of the base surface. The cellular model is used to calculate the trendline "Model" (dashed line), with $C = 0.17$ used to fit the data to the model. Other parameters used include: $R_{out} = 4$ nm, $R_{in} = 2$ nm, and $E_s = 0.9$ TPa. α and f are determined from image data for each point. The horizontal error bars include the standard deviation of α and the vertical error bars include the error due to the standard deviations of E_2 and f for each point.

Finally, these results can be used to predict elastic modulus and Fig. 9 shows the expected local in-plane and out-of-plane moduli throughout the thickness of a VACNT film, calculated using the foam model with parameters extracted from image data and C determined from data fitting. As expected, E_2 peaks in the middle region and is lowest at the base. E_1 and E_2 begin to converge at the base as the CNTs become more misaligned. E_1 is much lower than E_2, which agrees with past data from Deck et al. [9] that showed that VACNT films are nearly five times stiffer when compressed in the out-of-plane direction than the in-plane direction. This also supports past work showing low in-plane "middle" region modulus of VACNT films grown under similar conditions as the films in this work [14]. Note that these results do not include analysis of the crust layer, which needs a different image analysis procedure. The low modulus of these films, particularly in the in-plane direction, reflects their potential suitability as compliant thermal interface materials.

4. Concluding remarks

We have observed the inhomogeneous structure of multi-walled VACNT films using image analysis and mechanical property measurements. Nanoindentation measurements are performed on both the top and base surfaces of VACNT films. Results show that E_2 varies significantly between the top and bottom surface, ranging from 1.0 to 2.8 MPa for the top surface and 0.2–1.4 MPa for the base. These data are

compared to a cellular model through analysis of the tube structure using properties observed from SEM images. While the cellular model can be improved, its simplicity is useful for understanding trends in film behavior based on the morphology of the tube structure. For further analysis, measurements can be performed on films with different structure, such as densified or unaligned films to observe the impact of greater variations in aspect ratio and density.

Acknowledgements

The authors would like to thank Professor Wei Cai for his help on creating and deriving the equations for the cellular model. This work was sponsored by the Office of Naval Research (N00014-09-1-0296-P00004, Dr. Mark Spector, program manager) and Bosch LLC, SRC, the MARCO IFC, and the National Science Foundation. We performed this work in part at the Stanford Nanofabrication Facility (a member of the National Nanotechnology Infrastructure Network), which is supported by the National Science Foundation under Grant ECS-Integrated Systems.

REFERENCES

[1] Prasher R. Thermal interface materials: historical perspective, status, and future directions. Proc IEEE 2006;94(8):1571–86.
[2] Gao Y, Marconnet A, Panzer M, LeBlanc S, Dogbe S, Ezzahri Y, et al. Nanostructured interfaces for thermoelectrics. J Electron Mater 2010;39(9):1456–62.
[3] Pop E, Mann D, Wang Q, Goodson K, Dai H. Thermal conductance of an individual single-wall carbon nanotube above room temperature. Nano Lett 2005;6(1):96–100.
[4] Tong T, Yang Z, Delzeit L, Kashani A, Meyyappan M, Majumdar A. Dense vertically aligned multiwalled carbon nanotube arrays as thermal interface materials. IEEE T Compon Pack T 2007;30(1):92–100.
[5] Mesarovic SD, McCarter CM, Bahr DF, Radhakrishnan H, Richards RF, Richards CD, et al. Mechanical behavior of a carbon nanotube turf. Scripta Mater. 2007;56(2):157–60.
[6] Zhang Q, Lu YC, Du F, Dai L, Baur J, Foster DC. Viscoelastic creep of vertically aligned carbon nanotubes. J Phys D: Appl Phys 2010;43(31):315401–7.
[7] McCarter CM, Richards RF, Mesarovic SD, Richards CD, Bahr DF, McClain D, et al. Mechanical compliance of photolithographically defined vertically aligned carbon nanotube turf. J Mater Sci 2006;41(23):7872–8.
[8] Zbib AA, Mesarovic SD, Lilleodden ET, McClain D, Jiao J, Bahr DF. The coordinated buckling of carbon nanotube turfs under uniform compression. Nanotechnology 2008;19(17):175704–10.
[9] Deck CP, Flowers J, McKee GSB, Vecchio K. Mechanical behavior of ultralong multiwalled carbon nanotube mats. J Appl Phys 2007;101(2):023512–23519.
[10] Cao A, Dickrell PL, Sawyer WG, Ghasemi-Nejhad MN, Ajayan PM. Super-compressible foamlike carbon nanotube films. Science 2005;310(5752):1307–10.
[11] Maschmann MR, Zhang Q, Du F, Dai L, Baur J. Length dependent foam-like mechanical response of axially indented vertically oriented carbon nanotube arrays. Carbon 2011;49(2):386–97.
[12] Maschmann MR, Zhang Q, Wheeler R, Du F, Dai L, Baur J. In situ SEM observation of column-like and foam-like CNT array nanoindentation. ACS Appl Mater Interf 2011;3(3):648–53.
[13] Tong T, Zhao Y, Delzeit L, Kashani A, Meyyappan M, Majumdar A. Height independent compressive modulus of vertically aligned carbon nanotube arrays. Nano Lett 2008;8(2):511–5.
[14] Won Y, Gao Y, Panzer MA, Dogbe S, Pan L, Kenny TW, et al. Mechanical characterization of aligned multi-walled carbon nanotube films using microfabricated resonators. Carbon 2012;50(2):347–55.
[15] Zhang L, Li Z, Tan Y, Lolli G, Sakulchaicharoen N, Requejo FG, et al. Influence of a top crust of entangled nanotubes on the structure of vertically aligned forests of single-walled carbon nanotubes. Chem Mater 2006;18(23):5624–9.
[16] Bedewy M, Meshot ER, Guo H, Verploegen EA, Lu W, Hart AJ. Collective mechanism for the evolution and self-termination of vertically aligned carbon nanotube growth. J Phys Chem C 2009;113(48):20576–82.
[17] Wang BN, Bennett RD, Verploegen E, Hart AJ, Cohen RE. Quantitative characterization of the morphology of multiwall carbon nanotube films by small-angle x-ray scattering. J Phys Chem C 2007;111(16):5859–65.
[18] Malik H, Stephenson K, Bahr D, Field D. Quantitative characterization of carbon nanotube turf topology by SEM analysis. J Mater Sci 2011;46(9):3119–26.
[19] Al-Khedher MA, Pezeshki C, McHale JL, Knorr FJ. Quality classification via Raman identification and SEM analysis of carbon nanotube bundles using artificial neural networks. Nanotechnology 2007;18(35):355703–13.
[20] Hutchens SB, Needleman A, Greer JR. Analysis of uniaxial compression of vertically aligned carbon nanotubes. J Mech Phys Solids 2011;59(10):2227–37.
[21] Hutchens SB, Hall LJ, Greer JR. In situ mechanical testing reveals periodic buckle nucleation and propagation in carbon nanotube bundles. Adv Funct Mater 2010;20(14):2338–46.
[22] Qi HJ, Teo KBK, Lau KKS, Boyce MC, Milne WI, Robertson J, et al. Determination of mechanical properties of carbon nanotubes and vertically aligned carbon nanotube forests using nanoindentation. J Mech Phys Solids 2003;51(11–12):2213–37.
[23] Barako MT, Gao Y, Marconnet AM, Asheghi M, Goodson KE, editors. Solder Bonding for carbon nanotube-based thermal interface materials. Thermal and Thermomechanical Phenomena in Electronic Systems (ITherm), 2012 13th IEEE Intersociety Conference on 2012; San Diego, CA.
[24] Sader JE, Chon JWM, Mulvaney P. Calibration of rectangular atomic force microscope cantilevers. Rev Sci Instrum 1999;70(10):3967–9.
[25] Kodama T, Ohtani H, Arakawa H, Ikai A. Atomic force microscope equipped with confocal laser scanning microscope for the spectroscopic measurement of the contact area in liquid. Chem Phys Lett 2004;385(5–6):507–11.
[26] Menčík J, Munz D, Quandt E, Weppelmann ER, Swain MV. Determination of elastic modulus of thin layers using nanoindentation. J Mater Res 1997;12:2475–84.
[27] Pailler-Mattei C, Bec S, Zahouani H. In vivo measurements of the elastic mechanical properties of human skin by indentation tests. Med Eng Phys 2008;30(5):599–606.
[28] Oyen ML. Handbook of Nanoindentation: with biological applications: Pan Stanford Publishing; 2010.
[29] Butt H-J, Cappella B, Kappl M. Force measurements with the atomic force microscope: technique, interpretation and applications. Surf Sci Rep 2005;59(1–6):1–152.
[30] Jaschke M, Butt H-J. Height calibration of optical lever atomic force microscopes by simple laser interferometry. Rev Sci Instrum 1995;66(2):1258–9.

[31] Heim L-O, Kappl M, Butt H-J. Tilt of atomic force microscope cantilevers: effect on spring constant and adhesion measurements. Langmuir 2004;20(7):2760–4.
[32] Oliver WC, Pharr GM. An improved technique for determining hardness and elastic modulus using load and displacement sensing indentation experiments. J Mater Res 1992;7:1564–83.
[33] Ebenstein DM, Wahl KJ. A comparison of JKR-based methods to analyze quasi-static and dynamic indentation force curves. J Colloid Interface Sci 2006;298(2):652–62.
[34] Zhao Y, Tong T, Delzeit L, Kashani A, Meyyappan M, Majumdar A. Interfacial energy and strength of multiwalled-carbon-nanotube-based dry adhesive. J Vacuum Sci Technol B: Microelectron Nanometer Struct 2006;24(1):331–5.
[35] Yurdumakan B, Raravikar NR, Ajayan PM, Dhinojwala A. Synthetic gecko foot-hairs from multiwalled carbon nanotubes. Chem Commun 2005;30:3799–801.
[36] Johnson KL, Kendall K, Roberts AD. Surface Energy and the contact of elastic solids. in: Proceedings of the Royal Society of London A Mathematical and Physical, Sciences; 1971 September 8 (1971), pp. 324 (1558), pp. 301–13.
[37] Tabor D. Surface forces and surface interactions. J. Colloid Interface Sci 1977;58(1):2–13.
[38] Jiang W-G, Su J-J, Feng X-Q. Effect of surface roughness on nanoindentation test of thin films. Eng Fract Mech 2008;75(17):4965–72.
[39] Walter C, Antretter T, Daniel R, Mitterer C. Finite element simulation of the effect of surface roughness on nanoindentation of thin films with spherical indenters. Surf Coat Technol 2007;202(4–7):1103–7.
[40] Suhr J, Victor P, Ci L, Sreekala S, Zhang X, Nalamasu O, et al. Fatigue resistance of aligned carbon nanotube arrays under cyclic compression. Nat Nano 2007;2(7):417–21.
[41] Kim J-Y, Kang S-K, Lee J-J. Kwon D. Influence of surface-roughness on indentation size effect. Acta Mater 2007;55(10):3555–62.
[42] Schneider F, Fellner T, Wilde J, Wallrabe U. Mechanical properties of silicones for MEMS. J Micromech Microeng 2008;18(6):065008–65016.
[43] Park S-J, Goodman MB, Pruitt BL. Analysis of nematode mechanics by piezoresistive displacement clamp. Proc Natl Acad Sci 2007;104(44):17376–81.
[44] Gibson LJ, Ashby MF. Cellular Solids: Structure and Properties. 2 ed. Cambridge, UK: Cambridge University Press; 1997.
[45] Demczyk BG, Wang YM, Cumings J, Hetman M, Han W, Zettl A, et al. Direct mechanical measurement of the tensile strength and elastic modulus of multiwalled carbon nanotubes. Mater Sci Eng, A 2002;334(1–2):173–8.
[46] Underwood EE. Quantitative stereology. Reading, MA: Addison–Wesley Publishing Co.; 1970.